ACS APPLIED MATERIALS & INTERFACES

Research Article

www.acsami.org

Thermal Cycling Behavior of Zinc Antimonide Thin Films for High Temperature Thermoelectric Power Generation Applications

Hyung Cheoul Shim,* Chang-Su Woo, and Seungwoo Han*

Department of Nano-Mechanics, Korea Institute of Machinery & Materials (KIMM), 156 Gajeongbuk-Ro, Yuseong-Gu, Daejeon 305-343, Republic of Korea

Supporting Information

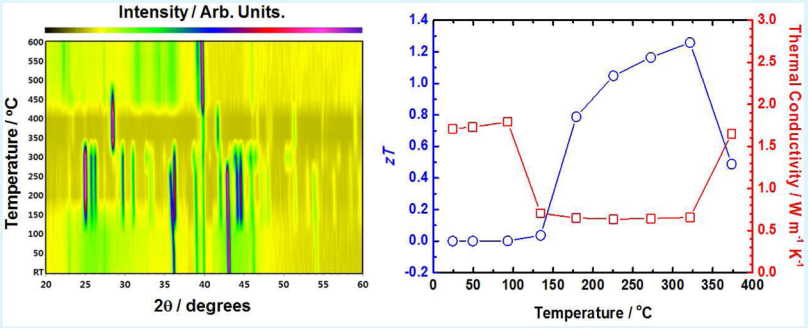

ABSTRACT: The zinc antimonide compound Zn_xSb_y is one of the most efficient thermoelectric materials known at high temperatures due to its exceptional low thermal conductivity. For this reason, it continues to be the focus of active research, especially regarding its glass-like atomic structure. However, before practical use in actual surroundings, such as near a vehicle manifold, it is imperative to analyze the thermal reliability of these materials. Herein, we present the thermal cycling behavior of Zn_xSb_y thin films in nitrogen (N_2) purged or ambient atmosphere. Zn_xSb_y thin films were prepared by cosputtering and reached a power factor of 1.39 mW m^{-1} K^{-2} at 321 °C. We found maximum power factor values gradually decreased in N_2 atmosphere due to increasing resistivity with repeated cycling, whereas the specimen in air kept its performance. X-ray diffraction and electron microscopy observations revealed that fluidity of Zn atoms leads to nanoprecipitates, porous morphologies, and even growth of a coating layer or fiber structures on the surface of Zn_xSb_y after repetitive heating and cooling cycles. With this in mind, our results indicate that proper encapsulation of the Zn_xSb_y surface would reduce these unwanted side reactions and the resulting degradation of thermoelectric performance.

KEYWORDS: *zinc antimonide, thermoelectric thin film, thermal cycle, thermoelectric properties and measurement, RF magnetron cosputtering*

INTRODUCTION

Recently, as an attempt to address growing environmental problems, research on energy alternatives to conventional fossil fuels has been actively promoted. In particular, the rapid development of electric vehicles (EVs) is an indicator that this trend is in full swing. However, with current EV technology, long-distance travel on a single charge is difficult compared to gasoline vehicles. Moreover, in the winter and summer seasons, the distance EVs can travel without recharging is shorter because an additional load is applied by the air conditioning system, which further limits their commercial adoption. Meanwhile, as the need for an auxiliary power generation system has increased, and to increase the efficiency of vehicles using conventional fuels, thermoelectric (TE) power generation technology has been attracting attention among many candidates due to its ability to utilize waste heat from the vehicle.[1,2] Generally, ∼60% of the energy generated in a conventional car is discarded as waste heat;[3,4] thus, it is possible to greatly improve the energy efficiency of the vehicle by taking advantage of the waste exhaust gas. A TE power generation system mounted near the engine or the exhaust pipe of an automobile can deliver additional energy using the Seebeck effect based on the large temperature difference.[1−4] BMW and Ford have reported that, in vehicle experiments involving such a TE power generation system, energy efficiency has been improved by ∼4% or more.[5,6]

Development of efficient TE materials is one of the key issues to building a thermoelectric power generation system because a material with good TE properties can produce additional power more effectively in a vehicle. The efficiency of TE materials, expressed as the value zT, is determined by $zT = \alpha^2 T \rho^{-1} \kappa^{-1}$, where α is the Seebeck coefficient, T is the absolute temperature, ρ is the electrical resistivity, and κ is the thermal conductivity. TE materials with a zT above 1.0 are

Received: May 18, 2015
Accepted: July 30, 2015
Published: July 30, 2015

DOI: 10.1021/acsami.5b04291
ACS Appl. Mater. Interfaces 2015, 7, 17866−17873

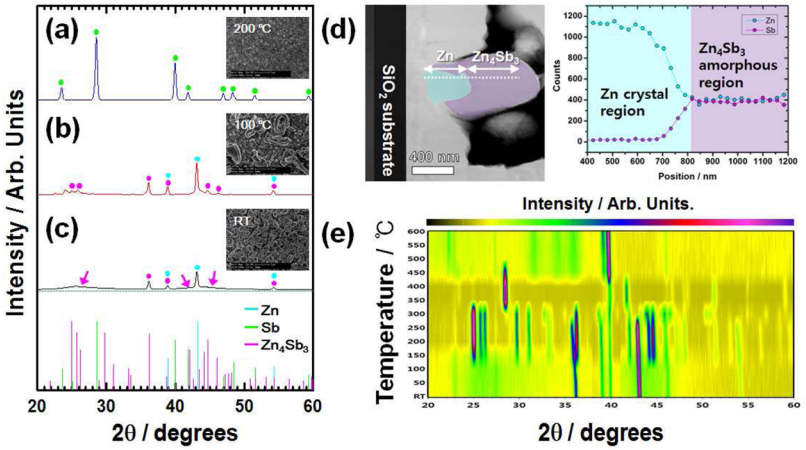

Figure 1. XRD patterns of samples deposited on the substrate at (a) 200 °C (Sb), (b) 100 °C (Zn + Zn_4Sb_3), and (c) room temperature (RT) (Zn + amorphous Zn_4Sb_3 (a-Zn_4Sb_3)). Top view FESEM images of the corresponding samples are presented in the inset of the figure. (d) STEM image and TEM-EDS line profile (from white dotted line on the STEM image) data of pristine sample (Zn + a-Zn_4Sb_3). (e) In situ high temperature XRD data from annealing of a Zn + a-Zn_4Sb_3 phase showing the phase transformation toward Zn_4Sb_3 from 130 to 350 °C, ZnSb from 350 to 450 °C, and Sb at >450 °C.

typically required for a TE device to achieve a reasonable efficiency for commercial application.[1] In most cases, due to the low efficiency of the TE material, the development rate of TE systems has been very slow. In recent years, however, as it has become possible to control phonon scattering with nanostructures, the development of high-efficiency TE materials has accelerated.[7,8] Among developed TE materials with a high zT value, bismuth telluride (Bi_2Te_3)-based systems have superior efficiency when operating near room temperature.[9−13] However, a TE material used for vehicle power generation must be able to perform well at high temperatures because the temperature at the manifold or engine block fluctuates around 300 °C.[1−6] Under those conditions, materials such as lead telluride (PbTe) or zinc antimonide (Zn_xSb_y) are more suitable for TE power generation than the conventional Bi_2Te_3-based systems, which have high efficiency at room temperature.[14−17] Among the high temperature materials, the zT value of Zn_xSb_y is very high compared to other substances due to the exceptionally low thermal conductivity of the material, which is associated with its glass-like structure.[16] There are experimental reports of an outstanding zT of ∼1.3 at around 670 K;[18,19] moreover, Zn_xSb_y compounds have a number of additional advantages, including being an environmentally friendly material that is relatively abundant, low cost, and less toxic than PbTe materials.[20] However, Zn_xSb_y undergoes structural changes in response to temperature, which has produced continuous stability problems.[21−23] Moreover, when the materials described above have been applied to real vehicle systems, their stability has not been evaluated properly, although they can be exposed to an ambient condition, not to an inert environment, with severe repetitive rapid changes at high temperature.

In this paper, we investigated the TE properties of Zn_xSb_y thin films under repetitive thermal cycling. In addition, we also measured the TE properties of Zn_xSb_y films under different atmospheric environments. We discovered that, as the number of thermal cycles increases, the power factor of Zn_xSb_y is reduced, and this degradation is more pronounced in an inert gas atmosphere than in ambient surroundings. The main cause of this degradation is closely related to the reduction in the electrical conductivity of the Zn_xSb_y thin film, which is associated with thermal decomposition, and this phenomenon was confirmed by various characterizations using X-ray diffraction (XRD) and transmission electron microscopy (TEM) analyses.

EXPERIMENTAL SECTION

Thin Film Deposition. Zn_xSb_y thin films were prepared by codeposition with high purity zinc and antimony (LTS chemical, 99.999%) on silicon dioxide (SiO_2) substrates in a radio frequency (RF) magnetron sputtering system (ATC ORION 5 UHV, AJA international, Inc.) at room temperature (RT) to 200 °C. The chamber base pressure was ∼2×10^{-7} Torr. Argon (Ar) was used as sputter-gas at a flow rate of 12 sccm, and the pressure in the chamber was fixed at 3.6 mTorr. To control the thin film growth, different RF powers of 28−60 W and a deposition time of 2 h were applied.

Characterization. The deposited thin films were then characterized using various methods. The thin film morphologies were studied using FE-SEM (Magellan400, FEI) and TEM (Tecnai F20 G^2, FEI). The TEM samples were prepared using focused ion beam (Nova 600 NanoLab, FEI) and a precision ion polishing system (PIPS). The diffraction patterns of the thin film samples were collected at 0.01° step widths over a 2θ range from 10° to 90° with an X-ray diffractometer (D/MAX-2500, RIGAKU) using Cu Kα radiation. The in situ high temperature X-ray diffraction patterns were collected at temperatures from RT to 600 °C with a heating rate of 5 °C/min in Ar-purged atmosphere. The in-plane Seebeck coefficient and electrical resistivity were simultaneously measured from RT to 500 °C under N_2 and air atmosphere using thermoelectric property measurement systems (SEEPEL Co., Ltd.).

RESULTS AND DISCUSSION

Panels a−c in Figure 1 show different XRD patterns of the Zn_xSb_y thin film deposited with varying substrate temperatures at fixed sputtering power conditions of 65 (Zn) and 30 (Sb) Watt (W) for 120 min. In addition, FESEM images, located at the right corner of each of the XRD patterns, show the top-view surface morphologies of the thin films.

In the XRD pattern in Figure 1c, the thin film deposited at room temperature (RT, type A) shows an almost amorphous Zn_4Sb_3 component with some reflections from Zn crystal. From the FESEM morphologies, we also observed that many round-shaped particles were embedded in the Zn_4Sb_3 matrix deposited at RT. These particles exhibit an interesting compositional

DOI: 10.1021/acsami.5b04291
ACS Appl. Mater. Interfaces 2015, 7, 17866−17873

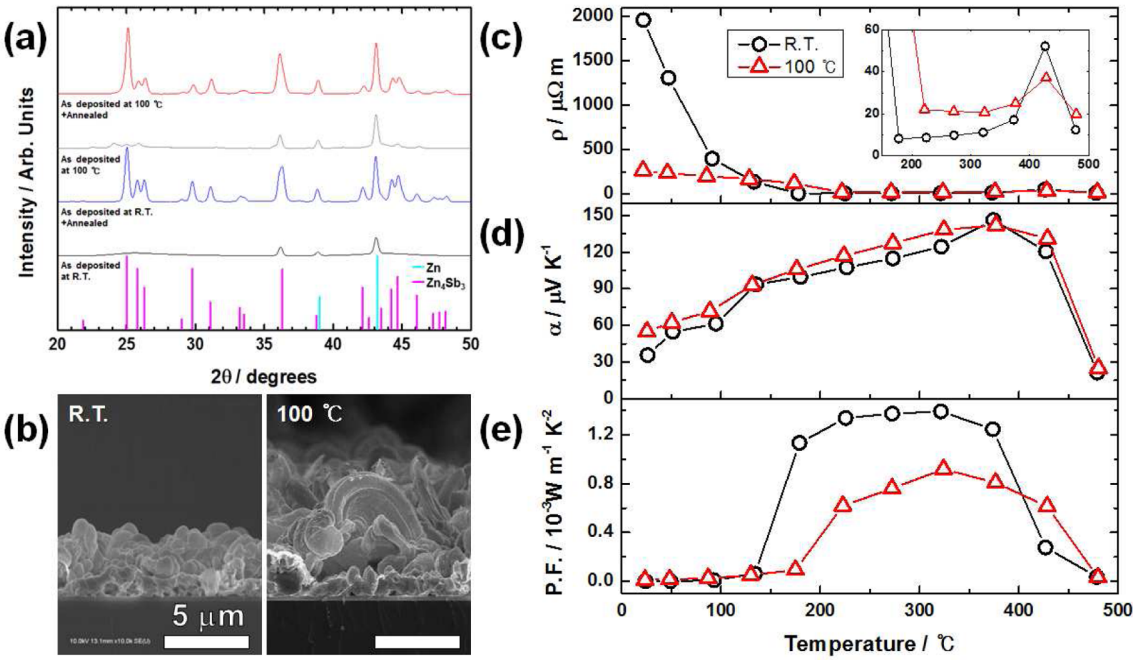

Figure 2. XRD patterns of samples deposited on the substrate at (a) room temperature (type A, gray line, Zn + amorphous Zn4Sb3 (a-Zn_4Sb_3)) and 100 °C (type B, light gray line, Zn + Zn_4Sb_3). The blue and red lines indicate the XRD patterns of type A and B samples, respectively, after annealing. (b) Cross-sectional FESEM images of type A (left) and B (right) samples. Thermoelectric properties of Zn_xSb_y thin film samples as a function of temperature for (c) resistivity (ρ), (d) Seebeck coefficient (α), and (e) power factor (P.F.) data.

segregation between Zn and Zn_4Sb_3, as shown in the cross sectional scanning TEM (STEM) image and TEM-energy dispersive spectroscopy (TEM-EDS) line profiling analysis (Figure 1d). The Zn does not exist as a solid solution form in the thin film matrix but is embedded as a segregated crystal structure in the amorphous Zn_4Sb_3 particles. This segregation could be induced by the relatively lower solubility of Zn than that of Sb at high temperature[24] or the growth of Zn precipitates from nucleation due to inhomogeneity of the substrate temperature.[25] At a substrate temperature of 100 °C, the Zn (101) peak was more developed, and amorphous Zn_4Sb_3 components were crystallized. The sharper Zn (101) peak can be related to not only the more crystallized Zn components in the Zn-rich Zn_4Sb_3 particles but also the noticeable growth of some chunks on the thin film, possibly reflecting the size reduction of Zn-rich Zn_4Sb_3 particles from around 2−3 μm to <1 μm (Figure 1b). These unusual residual chunks on the surface of the thin film were identified by SEM-EDS analysis as being comprised mostly of Zn (~97.22 atomic %).

As mentioned above, the solubility of Zn in Zn_4Sb_3 decreases with increasing temperature;[24] hence, the insoluble Zn component formed some islands on the thin film due to their limited solubility at 100 °C. Moreover, from the SEM-EDS analysis, the total atomic % of Zn in the Zn-rich Zn_4Sb_3 particle also decreased by ~7.87% as compared to that in the particles formed at RT. Therefore, it is possible to speculate that at high temperature the insoluble Zn component might form some Zn chunks on the thin film, and consequently, lead to a relative Zn deficiency in the Zn-rich Zn_4Sb_3 particles, in contrast to the case at RT.

Finally, we characterized thin films that were deposited at a substrate temperature of 200 °C. The XRD and SEM-EDS data showed only the Sb component in the thin film. Thus, for further measurement of thermoelectric properties, we chose the thin film samples that were deposited on the substrate at a temperature under 200 °C.

Generally, bulk β-Zn_4Sb_3 is known to be stable in the temperature range between 263 and 765 K;[28] however, this can be changed depending on impurity contents, dimensionality, and so forth.[29−32] Thus, before we investigated the phase transition of the Zn_xSb_y thin film with increasing temperature, we utilized the in situ high temperature X-ray diffractometer at a temperature range from RT to 600 °C in Ar-purged atmosphere. The 2D XRD patterns in Figure 1e show the clear phase evolution of the type A sample with increasing temperature. At a temperature less than ~130 °C, the Zn (101) peak near 43° dominates the XRD patterns, and the β-Zn_4Sb_3 phase including the (030) peak starts to develop above 150 °C. The Zn (101) peak was nearly smeared above 300 °C, whereas the β-Zn_4Sb_3 phase still remained, and its phase stability was maintained around 350 °C.

However, its phase suddenly changed toward ZnSb at a temperature >350 °C, and finally, only the Sb component remained over 470 °C. Conversely, the thin film grown at a substrate temperature of 100 °C (type B) showed β-Zn_4Sb_3 evolution at a starting temperature ~50 °C higher than that of type A (Figure S1a). Moreover, the quantitative XRD analysis showed that the weight % composition of β-Zn_4Sb_3 in type B thin films over all temperature ranges was also ~12.5% lower than that of type A (Figure 1b), suggesting that the excessive Zn component in type B may be hindered in phase transition toward β-Zn_4Sb_3. Eventually, the experimental results for thin films at the different substrate temperatures mirrored their thermoelectric (TE) properties, which will be discussed later (Figure 2c−e). Another factor to be addressed is related to the upper thermal stability limit of the β-Zn_4Sb_3 thin film, which was much lower than that of the bulk material (~492 °C), suggesting dimensionality has a considerable effect on the thermal stability of the material. From that point of view, the

DOI: 10.1021/acsami.5b04291
ACS Appl. Mater. Interfaces 2015, 7, 17866−17873

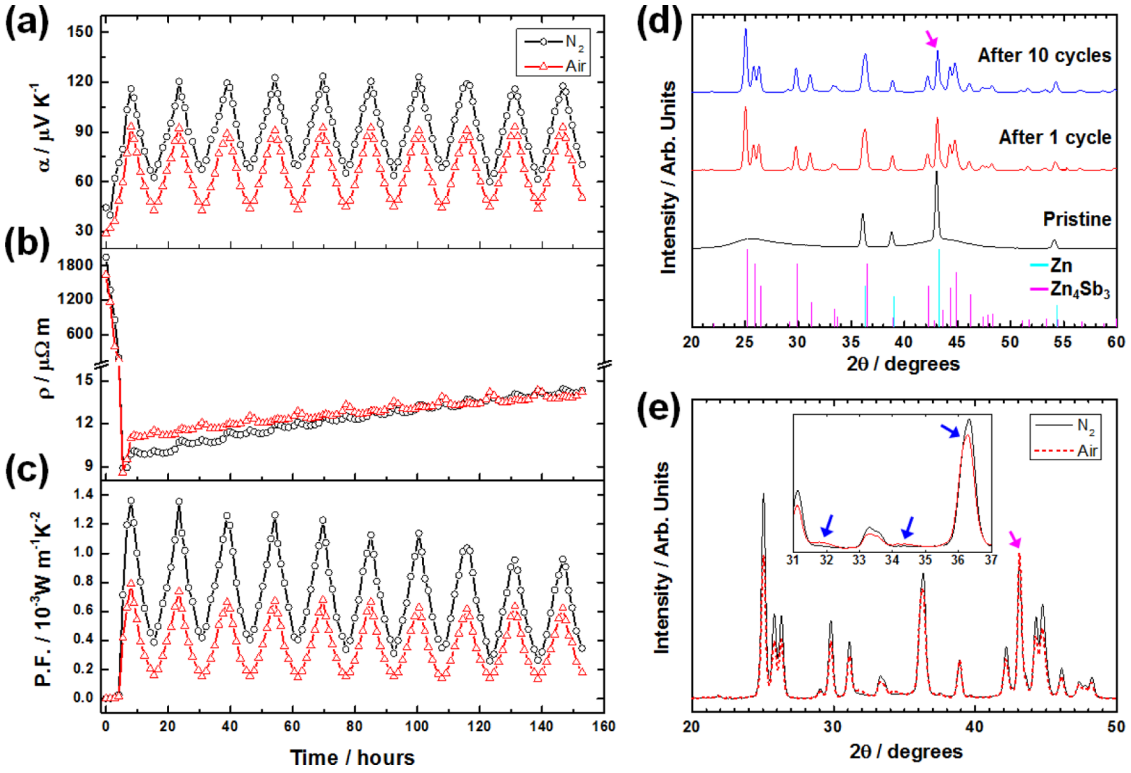

Figure 3. (a) Seebeck coefficient (α), (b) resistivity (ρ), and (c) power factor (P.F.) of the Zn_xSb_y thin film of a type A sample (Zn + a-Zn_4Sb_3). Ten measurement cycles in the temperature range of RT to 300 °C were performed in N_2 (black) or air (red). (d) XRD patterns of the type A pristine sample (black line) after the first thermal cycle (red line) and after 10 cycles (blue line). The pink arrow shows the decrease in the Zn (101) peak after 10 thermal cycles due to Zn deficiency by thermal decomposition. (e) XRD patterns of the type A sample after 10 thermal cycles in N_2 (black line) and air (red dotted line). The blue and pink arrows reflect the ZnO and Zn (101) peaks, respectively. Specifically, the pink arrow indicates the increase in the Zn (101) peak of a type A sample after 10 thermal cycles in air due to the growth of Zn precipitates, in contrast to when the sample was subjected to thermal cycling in N_2 atmosphere, which produces a decrease in the Zn (101) peak, as shown in (d).

experimental conditions of the post treatment process have to be very carefully considered when dealing with a low dimensional material instead of conventional bulk TE materials. Thus, we decided the temperature range for a thermal cycling test of the Zn_xSb_y thin film should be from RT to 300 °C based on the in situ high temperature XRD data.

Figure 2a shows the XRD pattern that was extracted from the in situ high temperature XRD data between RT and 270 °C (Figure 1e). After heat treatment, even with the different sputtering condition of substrate temperature at RT and 100 °C, they show very similar XRD patterns, unlike the XRD patterns of the as deposited film. However, according to a quantitative analysis based on XRD data, the proportion of Zn in the type B thin film is ~2.6× higher than that of type A. As mentioned before, this excessive Zn component hampered the phase transition toward β-Zn_4Sb_3, and it may mirror the increased resistivity (ρ) of the thin film over 200 °C (Figure 2c). Actually, in the temperature range between RT and 133 °C, the measured ρ of type B is much lower than that of RT because of excessive Zn chunks on the thin film, as we mentioned in Figure 1b. However, above 178 °C, these Zn residuals negatively influence the conductivity of the thin film. As shown in Figure 2b, the as grown Zn chunks break the thin film, which might lead to a decrease in the conductivity of the thin film with increasing temperature. Consequently, type B shows a lower power factor (P.F.) value of 0.92 mW m^{-1} K^{-2} compared to that of type A, which has a P.F. of 1.39 mW m^{-1} K^{-2} due to its lower conductivity at 321 °C, even though it has a slightly higher Seebeck coefficient (α) value than type A. Moreover, as shown in the in situ high temperature XRD pattern, type B contains less β-Zn_4Sb_3 component than type A (Figure S1b), and the thermoelectric efficiency is also poor due to its higher thermal conductivity (κ), which is related to the excessive Zn component. Actually, because we estimated zT values versus temperature for the type A thin film based on κ values of the corresponding bulk materials,[16,33,34] the samples of course indicate a maximum zT value of 1.26 at 321 °C, which is associated with the maximum content of β-Zn_4Sb_3 in the thin film, and a minimum zT value of 2.64×10^{-4} at 24 °C when it had the maximum Zn content (Figure S2b). However, the P.F. value of type B above 427 °C is higher than that at RT. This is related to the interesting sudden ρ drop above 426 °C, which is possibly due to melted Zn (the melting point of Zn is ~420 °C) connected to percolating paths along the grain boundaries.[28] The porous morphologies along the grain boundaries are shown in the TEM image in Figure S2a, which was obtained after measurement of TE properties and also supports the likelihood of this phenomenon.

Panels a–c in Figure 3 show the TE properties of type A measured after being subjected to thermal cycling 10 times. The thermal cycling temperature range was from RT to 300 °C, and based on the in situ high temperature XRD data, the maximum temperature was limited to <300 °C to impede the phase transition from β-Zn_4Sb_3 to other materials, such as ZnSb or Sb alone. The sample was heated with a heating rate of 2 °C min^{-1} and cooled to RT naturally in air or a nitrogen (N_2)-purged atmosphere. With increasing temperature, the α was increased and ρ decreased, which is general p-type semi-

DOI: 10.1021/acsami.5b04291
ACS Appl. Mater. Interfaces 2015, 7, 17866–17873

conducting behavior.[18] During the first thermal cycle in N_2, ρ quickly dropped from 1944.1 to 8.9 $\mu\Omega$ m, and then gradually increased with the number of cycles. The apparent decrease of ρ value during the first heating process in N_2 could be associated with crystallization followed by an annealing effect. We also believe that the gradual increase of ρ after the first cycle is possibly related to Zn deficiency. As shown in the XRD pattern in Figure 3d, the dominating Zn (101) peak in the Zn_xSb_y thin film decreases after 10 thermal cycles. This suggests that Zn is removed from the thin film matrix as thermal cycling occurs, and this can be related to the increasing ρ value in Figure 3b. However, as shown in Figure 3a, there are few changes in the α value according to the thermal cycling with identical fluctuations with temperature variation. For this reason, the P.F. of the Zn_xSb_y thin film gradually decreases with the number of cycles.

Another possible cause for this P.F. value degradation is the development of internal defects, such as nano voids, and crack propagation during thermal cycling. Figure 4a displays the cross

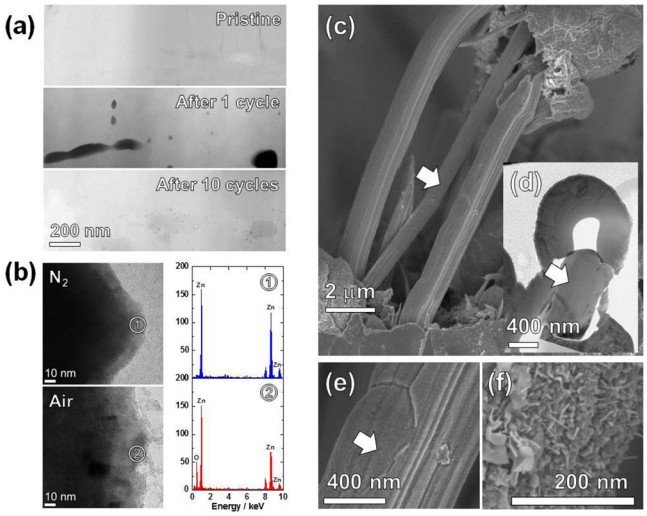

Figure 4. (a) STEM images of the type A sample (top) after the first thermal cycle (middle) and after 10 cycles (bottom). (b) TEM images of the type A sample after 10 thermal cycles in N_2 (top) and air (bottom). The TEM-EDS spectra was obtained from zone (1) (Zn) and zone (2) (Zn and O). (c) FESEM and (d) TEM image of Zn fiber (white arrow) on the type A sample after 5 thermal cycles in air. (e) Magnified FESEM image of the Zn fiber shown in (c). (f) FESEM image of a mixture of nano rod- and plate-like shaped ZnO, which was grown at the surface of a Zn fiber after 10 thermal cycles in air.

sectional STEM images of the Zn_xSb_y thin film after thermal cycling in N_2. After the first heating and quenching process, we observed many voids with sizes of 10−200 nm inside the thin film. These voids were generated from the Zn precipitate inside of the Zn_4Sb_3 matrix.

Actually, the location of the segregated Zn component in a Zn-rich Zn_4Sb_3 particle was almost identical to the position of the void in the particle (Figure S3a). It is well-known that Zn has a very high diffusion rate in β-Zn_4Sb_3, as Zn moves easily from one interstitial site to the other.[24,26,35] Therefore, at maximum temperature during the heating process, zinc atoms with high mobility are able to escape to the surface of the Zn_4Sb_3 matrix, leaving the voids.[24,26−28] TEM images and TEM-EDS analysis in Figure 4b confirm this phenomenon, as the escaped zinc atoms form a Zn coating layer of 10 nm on the surface of the Zn_4Sb_3 thin film. Moreover, this is also supported by SEM-EDS analysis (Figure 5d), which shows a gradual increase of the Zn composition at the surface, whereas it is reduced inside the thin film sample with increasing numbers of thermal cycles.

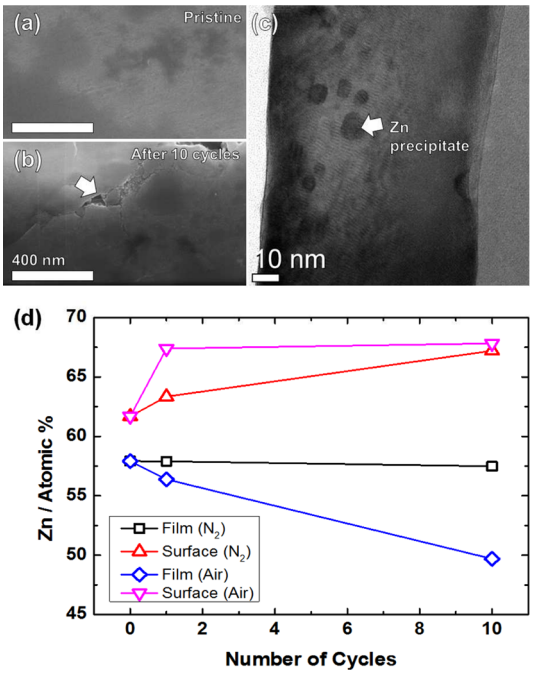

Figure 5. Cross-sectional FESEM image of type A (a) pristine thin film and (b) after 10 thermal cycles in N_2. The white arrow shows the growth of internal cracks of the thin film due to thermal stress during the measurement cycling. (c) TEM image of type A sample after 10 thermal cycles in air. The repetitive heating and quenching cycles lead the mobile Zn atoms to form aggregates and Zn precipitates (white arrow) inside of the thin film. (d) SEM-EDS results of the type A thin film according to the number of thermal cycles. "Film" and "Surface" mean that the EDS spot is located at the middle and near the surface of the cross-sectional thin film, respectively.

Interestingly, after 10 cycles, the size of these voids decreased to <10 nm, and their positions were rearranged along the grain boundaries as shown in the TEM image of Figure 4a. This can be explained as follows: when the sample is subsequently heated upon annealing, the Zn solubility is higher, and Zn can re-enter the Zn_4Sb_3 phase from the inclusions.[24,26,27] Thus, the Zn in the Zn_xSb_y, with its higher solubility, can move around easily in the thin film matrix after the second cycle because it was already annealed during the first cycle. For this reason, the voids of a few hundred nanometers might be reduced by filling with re-entered Zn or be shrunk by the crystal growth of neighboring grains during the repetitive heating process.

In addition, the Zn prefers to diffuse along the grain boundaries in an attempt to minimize energy, and this could be proposed as the main mechanism for the rearrangement of many nano voids along the grain boundaries after 10 thermal cycles. These nano voids might block the carrier flow of the Zn_xSb_y thin film, which could induce the increasing resistivity of the sample. Also, repetitive annealing and quenching could apply thermal stress to the inside of the thin film. Actually, we observed many cracks on the inside of the thin film after thermal cycling (Figure 5b), and they could be produced by the difference in thermal coefficient value between the TE thin

DOI: 10.1021/acsami.5b04291
ACS Appl. Mater. Interfaces 2015, 7, 17866−17873

material and SiO_2/Si substrate.[39] Therefore, besides the removal of the Zn component from the sample through thermal decomposition (See Figure S4), the generation of nano voids and cracks induced by thermal stress could also be responsible for the gradual decrease in the power factor value of the Zn_xSb_y thin film under repetitive heating and quenching treatment, as shown in Figure 3c.

The thin film heated in air also showed a similar reduction in ρ during the first heating cycle but gave rise to higher ρ during the quenching process, as compared to that heated in N_2. This could be attributed to the generation of zinc oxide (ZnO), which could be formed when Zn, removed from the thin film matrix, was exposed to oxygen (O_2) in air. Actually, after thermal cycling in air, there was a slight emergence of small XRD peaks that reflect the ZnO (100), (002), and (101) at 31.8°, 34.4°, and 36.3°, respectively, as shown in the inset to Figure 3e.

Similarly, after 10 thermal cycles, we also observed that the surface of a sample heated in air was covered with a ZnO layer, as shown in Figure 4b, which is in good agreement with the presence of ZnO peaks in the XRD patterns of Figure 3e. In addition, as compared with a sample heated and quenched in N_2, the XRD peaks reflecting Zn_4Sb_3 were reduced overall after atmospheric thermal cycling. Whereas the Zn (101) peak is rather to be is increased after thermal cycling relative to the as deposited thin film, mirroring very strong thermal decomposition of Zn_4Sb_3 that can have a relatively low α value in air, as shown in Figure 3a.

However, the ZnO layer at the surface of the thermoelectric thin film might lead to the retention of a higher P.F. value during thermal cycling. As shown in Figure 3c, on the basis of the maximum P.F. value, when the thin film was subjected to the ambient process, 78.6% of the initial P.F. value was maintained after 10 cycles, whereas the sample in N_2 retained 70.4% of its initial P.F. value (see Figure S7). Of course, with further cycling, the sample under the ambient process would fail because it would have a more rapid and stronger thermal decomposition of the Zn_xSb_y thin film than the sample processed in the N_2 atmosphere. This thermal decomposition leads to vibrant morphological changes inside the Zn_xSb_y thin film during the thermal cycling, which can be associated with film destruction.

Panels c–f in Figure 4 exhibit noticeable morphological changes in the Zn_xSb_y thin film after 10 thermal cycles in air. The zinc columns break through the thin film during the thermal cycle in air (Figure 4d) and even grow to a few micrometer scale. Moreover, as the thermal cycling proceeds in air, the plate-shaped ZnO additionally grows at the surface of the Zn columns (Figure 4f). We believe that the growth of fiber-like Zn structures is possibly related to stress relaxation of the thin film during the thermal cycling, followed by the generation of a ZnO layer at the surface of Zn_xSb_y. The main cause of increasing compressive stress might be the difference in thermal conductivity between the substrate (SiO_2/Si) and thin film (Zn_xSb_y), such that the Zn fiber grows on the thin film to relieve stress when it cools down.[39] In addition, the ZnO layer might accelerate this kind of side reaction that leads to the growth of the Zn fiber. Actually, we observed many Zn precipitates or segregated Zn regions (see Figures S5 and S6) after ambient thermal cycling, which never occurred in pristine or after the first thermal cycle (Figure 5c). However, when the thin films were subjected to thermal cycles in N_2, there was no Zn fiber, unlike that in the ambient conditions. These phenomena can be explained as follows: in N_2 atmosphere, the movable Zn atoms were able to evaporate out from the sample when they were heated and to form the amorphous Zn layer at the surface, as shown in Figure 3b. Consequently, the Zn component at the surface of the Zn_xSb_y thin film during thermal cycling in N_2 shows a gradual increase with an increasing number of cycles, as depicted in Figure 5d. Conversely, in an ambient environment, even though the sample was subjected to 10 thermal cycles, once the Zn component has increased at the surface, Zn quantities do not increase further. This is because once the evaporated Zn reacts with oxygen in air a ZnO layer is formed that possibly makes it difficult for further Zn to escape from the surface of the thin film matrix due to size exclusion given the atomic radius of O (0.140 nm) relative to Zn (0.074 nm).[38] Moreover, on the inside of the thin film, the ambient thermal cycle process leads to a rapid decrease in Zn quantity as compared to a sample in N_2 (Figure 5d). According to previous research, the thermal decomposition of Zn_4Sb_3 can generate ZnSb and Zn, or Zn and Sb, and the former degradation process is known to be intrinsic to the structure, whereas the latter is a faster and more common reaction for samples heated in air.[31,35−37] For this reason, the Zn thermally decomposed in air might drive the aggregation and growth of Zn precipitates on the inside of the thin film, and finally, growths of fiber-like Zn column structures can burst out from the matrix, relieving the compressive stress,[39] as shown in Figure 4d. Therefore, side effects, such as the oxidation of the thermoelectric thin film during thermal cycling, can give rise to the destruction of the device or severe degradation of thermoelectric performance with respect to thermal reliability.

Therefore, reducing residual thermal stress or blocking further internal agglomeration of the Zn component by using the layer-by-layer deposition (coating layer-thermoelectric layer-coating layer-...) technique would be helpful to prevent sample destruction under ambient thermal cycling. With this in mind, our conclusion is that proper surface coating or activation of the surface of the thermoelectric thin film material would reduce these unwanted side reactions and thermoelectric performance loss during repetitive thermal cycling, and this step is essential for the application of thermoelectric materials in actual surroundings, not just in a laboratory environment, which has a simple thermal profile.

CONCLUSIONS

In summary, we investigate the thermoelectric performance and microstructure evolution of Zn_xSb_y thin films subjected to thermal cycling. The high temperature in situ XRD patterns and TEM results show that the degradation in thermoelectric performance of the Zn_xSb_y thin film with an increasing number of thermal cycles comes from structural, morphological, and compositional changes. In particular, the fluidity of Zn atoms in the Zn_xSb_y thin film matrix during thermal cycling give rise to morphological and compositional changes, such as nano inclusions or voids, which leads to degradation of the thermoelectric performance over increasing thermal cycles. Moreover, these changes are more developed under atmospheric measurement conditions, which generate thermally decomposed Zn or other impurity phases. For instance, the ZnO coating layer, which comes from oxidation of thermally decomposed Zn from the Zn_xSb_y thin film, maintains the thermoelectric performance for some time by blocking Zn evaporation from the Zn_xSb_y thin film. However,the Zn_xSb_y thin film was eventually broken by growth of the Zn fiber to

DOI: 10.1021/acsami.5b04291
ACS Appl. Mater. Interfaces 2015, 7, 17866−17873

relieve the thermal stress, which was followed by Zn agglomeration with further atmospheric thermal cycling. These results provide insight for the needs for the proper encapsulation of the Zn_xSb_y surface that does not degrade thermoelectric performance with repeated thermal cycling.

■ ASSOCIATED CONTENT

Supporting Information

The Supporting Information is available free of charge on the ACS Publications website at DOI: 10.1021/acsami.5b04291.

Additional in situ high temperature XRD data, quantitative analysis from XRD data, STEM images, TEM images, and SAD patterns of zinc antimonide thin film (PDF)

■ AUTHOR INFORMATION

Corresponding Authors

*Tel: +82-42-868-7143. E-mail: scafos@kimm.re.kr.
*E-mail: swhan@kimm.re.kr.

Notes

The authors declare no competing financial interest.

■ ACKNOWLEDGMENTS

This work was supported by the Korea Institute of Machinery and Materials funding for "Development of flexible and stretchable energy device based on nano materials & mechanics technologies (NK188C)." The authors also would like to thank AAC (Advanced Analysis Center) of KIST (Korea Institute of Science and Technology) for their help in TEM analysis.

■ REFERENCES

(1) Bell, E. Cooling, Heating, Generating Power, and Recovering Waste Heat with Thermoelectric Systems. *Science* **2008**, *321*, 1457−1461.

(2) Yang, J. Potential Applications of Thermoelectric Waste Heat Recovery in the Automotive Industry. *Proceedings of 24th International Conference on Thermoelectrics (ICT)* **2005**, *2005*, 170−174.

(3) Yu, C.; Chau, T. Thermoelectric Automotive Waste Heat Energy Recovery using Maximum Power Point Tracking. *Energy Convers. Manage.* **2009**, *50*, 1506−1512.

(4) Stabler, F. Automotive applications of High Efficiency Thermoelectrics. *DARPA/ONR Program Review and DOE High Efficiency Thermoelectric Workshop*; San Diego, CA, March, 2002.

(5) Crane, T.; LaGrandeur, W. Progress Report on BSST-Led US Department of Energy Automotive Waste Heat Recovery Program. *J. Electron. Mater.* **2010**, *39*, 2142−2148.

(6) Fairbanks, W. In *Thermoelectrics for Vehicle Applications, Vehicular Thermoelectrics: A New Green Technology*, Diesel Engine-Efficiency and Emissions Research (DEER) Conference Presentations, Detroit, MI, Oct 3−6, 2011.

(7) Vineis, J.; Shakouri, A.; Majumdar, A.; Kanatzidis, G. Nanostructured Thermoelectrics: Big Efficiency Gains from Small Features. *Adv. Mater.* **2010**, *22*, 3970−3980.

(8) Nielsch, K.; Bachmann, J.; Kimling, J.; Böttner, H. Thermoelectric Nanostructures: From Physical Model Systems towards Nanograined Composites. *Adv. Energy Mater.* **2011**, *1*, 713−731.

(9) Venkatasubramanian, R.; Siivola, E.; Colpitts, T.; O'Quinn, B. Thin-Film Thermoelectric Devices with High Room-temperature Figures of Merit. *Nature* **2001**, *413*, 597−602.

(10) Poudel, B.; Hao, Q.; Ma, Y.; Lan, C.; Minnich, A.; Yu, B.; Yan, X.; Wang, D.; Muto, A.; Vashaee, D.; Chen, Y.; Liu, M.; Dresselhaus, S.; Chen, G.; Ren, Z. High-Thermoelectric Performance of Nanostructured Bismuth Antimony Telluride Bulk Alloys. *Science* **2008**, *320*, 634−638.

(11) Tang, F.; Xie, J.; Li, H.; Zhao, Y.; Zhang, J.; Niino, M. Preparation and Thermoelectric Transport Properties of High-Performance *p*-type Bi_2Te_3 with Layered Nanostructure. *Appl. Phys. Lett.* **2007**, *90*, 012102.

(12) Xie, W.; Tang, X.; Yan, Y.; Zhang, Q.; Tritt, M. Unique Nanostructures and Enhanced Thermoelectric Performance of Melt-Spun BiSbTe Alloys. *Appl. Phys. Lett.* **2009**, *94*, 102111.

(13) Xie, W.; Tang, X.; Yan, Y.; Zhang, Q.; Tritt, M. High Thermoelectric Performance BiSbTe Alloy with Unique Low-Dimensional Structure. *J. Appl. Phys.* **2009**, *105*, 113713.

(14) Heremans, P.; Jovovic, V.; Toberer, S.; Saramat, A.; Kurosaki, K.; Charoenphadee, A.; Yamanaka, S.; Snyder, J. Enhancement of Thermoelectric Efficiency in PbTe by Distortion of the Electronic Density of States. *Science* **2008**, *321*, 554−557.

(15) Yu, B.; Zhang, Q.; Wang, H.; Wang, X.; Wang, H.; Wang, D.; Wang, H.; Snyder, J.; Chen, G.; Ren, F. Thermoelectric Property Studies on Thallium-Doped Lead Telluride Prepared by Ball Milling and Hot Pressing. *J. Appl. Phys.* **2010**, *108*, 016104.

(16) Snyder, J.; Christensen, M.; Nishibori, E.; Caillat, T.; Iversen, B. Disordered Zinc in Zn_4Sb_3 with Phonon-Glass and Electron-Crystal Thermoelectric Properties. *Nat. Mater.* **2004**, *3*, 458−463.

(17) Snyder, J.; Toberer, S. Complex Thermoelectric Materials. *Nat. Mater.* **2008**, *7*, 105−114.

(18) Sun, Y.; Christensen, M.; Johnsen, S.; Nong, V.; Ma, Y.; Sillassen, M.; Zhang, E.; Palmqvist, C.; Bottiger, J.; Iversen, B. Low-Cost High-Performance Zinc Antimonide Thin Films for Thermoelectric Applications. *Adv. Mater.* **2012**, *24*, 1693−1696.

(19) Ahn, H.; Oh, W.; Kim, S.; Park, D.; Min, K.; Lee, W.; Shim, J. Thermoelectric Properties of Zn_4Sb_3 Prepared by Hot Pressing. *Mater. Res. Bull.* **2011**, *46*, 1490−1495.

(20) Amatya, R.; Ram, J. Trend for Thermoelectric Materials and Their Earth Abundance. *J. Electron. Mater.* **2012**, *41*, 1011−1019.

(21) Mozharivskyj, Y.; Pecharsky, O.; Bud'ko, S.; Miller, J. A Promising Thermoelectric Material: Zn_4Sb_3 or $Zn_{6-\delta}Sb_5$. Its Composition, Structure, Stability, and Polymorphs. Structure and Stability of $Zn_{1-\delta}Sb$. *Chem. Mater.* **2004**, *16*, 1580−1589.

(22) Cox, A.; Toberer, S.; Levchenko, A.; Brown, R.; Snyder, J.; Navrotsky, A.; Kauzlarich, S. M. Structure, Heat Capacity, and High-Temperature Thermal Properties of $Yb_{14}Mn_{1-x}Al_xSb_{11}$. *Chem. Mater.* **2009**, *21*, 1354−1360.

(23) Snider, S.; Badding, V.; Schujman, B.; Slack, A. High-Pressure Stability, Pressure-Volume Equation of State, and Crystal Structure under Pressure of the Thermoelectric Material $IrSb_3$. *Chem. Mater.* **2000**, *12*, 697−700.

(24) Rauwel, P.; Løvvik, M.; Rauwel, E.; Taftø, J. Nanovoids in Thermoelectric β-Zn_4Sb_3: A Possibility for Nanoengineering *via* Zn Diffusion. *Acta Mater.* **2011**, *59*, 5266−5275.

(25) Zhang, T.; Tsutsui, M.; Ito, K.; Yamaguchi, M. Thermoelectric Properties of Zn_4Sb_3 Thin Films Prepared by Magnetron Sputtering. *Thin Solid Films* **2003**, *443*, 84−90.

(26) Rauwel, P.; Løvvik, M.; Rauwel, E.; Toberer, S.; Snyder, J.; Taftø, J. Nanostructuring in β-Zn_4Sb_3 with Variable Starting Zn Compositions. *Phys. Status Solidi A* **2011**, *208*, 1652−1657.

(27) Lin, J.; Qiao, G.; Ma, L.; Ren, Y.; Yang, B.; Fei, Y.; Lei, L. Heterogeneous *in-situ* Nanostructure Contributes to the Thermoelectric Performance of Zn_4Sb_3. *Appl. Phys. Lett.* **2013**, *102*, 163902.

(28) Lin, J.; Li, X.; Qiao, G.; Wang, Z.; Carrete, J.; Ren, Y.; Ma, L.; Fei, Y.; Yang, B.; Lei, L.; Li, J. Unexpected High-Temperature Stability of β-Zn_4Sb_3 Opens the Door to Enhanced Thermoelectric Performance. *J. Am. Chem. Soc.* **2014**, *136*, 1497−1504.

(29) Pomrehn, S.; Toberer, S.; Snyder, J.; Walle, A. Entropic Stabilization and Retrograde Solubility in Zn_4Sb_3. *Phys. Rev. B: Condens. Matter Mater. Phys.* **2011**, *83*, 094106.

(30) Pomrehn, S.; Toberer, S.; Snyder, J.; Walle, A. Predicted Electronic and Thermodynamic Properties of a Newly Discovered Zn_8Sb_7 Phase. *J. Am. Chem. Soc.* **2011**, *133*, 11255−11261.

(31) Pedersen, L.; Iversen, B. Thermally Stable Thermoelectric Zn_4Sb_3 by Zone-Melting Synthesis. *Appl. Phys. Lett.* **2008**, *92*, 161907.

DOI: 10.1021/acsami.5b04291
ACS Appl. Mater. Interfaces 2015, 7, 17866−17873

(32) Schlecht, S.; Erk, C.; Yosef, M. Nanoscale Zinc Antimonides: Synthesis and Phase Stability. *Inorg. Chem.* **2006**, *45*, 1693−1697.
(33) Toberer, S.; Rauwel, P.; Gariel, S.; Tafto, J.; Snyder, J. Composition and the Thermoelectric Performance of β-Zn_4Sb_3. *J. Mater. Chem.* **2010**, *20*, 9877−9885.
(34) Caillat, T.; Fleurial, P.; Borshchevsky, A. Preparation and Thermoelectric Properties of Semiconducting Zn_4Sb_3. *J. Phys. Chem. Solids* **1997**, *58*, 1119−1125.
(35) Iversen, B. Fulfilling Thermoelectric Promises: β-Zn_4Sb_3 from Materials Research to Power Generation. *J. Mater. Chem.* **2010**, *20*, 10778−10787.
(36) Mozharivskyj, Y.; Janssen, Y.; Harringa, L.; Kracher, A.; Tsokol, O.; Miller, J. $Zn_{13}Sb_{10}$: A Structural and Landau Theoretical Analysis of Its Phase Transitions. *Chem. Mater.* **2006**, *18*, 822−831.
(37) Zhang, T.; Tsutsui, M.; Ito, K.; Yamaguchi, M. Effects of ZnSb and Zn Inclusions on the Thermoelectric Properties of β-Zn_4Sb_3. *J. Alloys Compd.* **2003**, *358*, 252−256.
(38) Zhaoyang, W.; Lizhong, H. Effect of Oxygen Pressure on the Structural and Optical Properties of ZnO Thin Films on Si (111) by PLD. *Vacuum* **2009**, *83*, 906−909.
(39) Ham, J.; Shim, W.; Kim, H.; Lee, S.; Roh, J.; Sohn, W.; Oh, H.; Voorhees, W.; Lee, W. Direct Growth of Compound Semiconductor Nanowires by On-Film Formation of Nanowires: Bismuth Telluride. *Nano Lett.* **2009**, *9*, 2867−2872.

DOI: 10.1021/acsami.5b04291
ACS Appl. Mater. Interfaces 2015, 7, 17866−17873